

# Energy absorption and damage propagation in 2D triaxially braided carbon fiber composites: effects of in situ matrix properties

Amit G. Salvi · Anthony M. Waas ·  
Ari Caliskan

Received: 26 January 2008 / Accepted: 25 April 2008 / Published online: 7 June 2008  
© Springer Science+Business Media, LLC 2008

**Abstract** Results from an experimental program to investigate the propagation of damage and energy dissipation in 2D triaxially braided carbon fiber textile composites (2DTBC) under static conditions are reported. A methodology is presented in which classical concepts from fracture mechanics are generalized to address damage growth in an orthotropic and heterogeneous structural material. Along with results from the experimental program, a novel numerical technique that employs ideas from cohesive zone modeling, and implemented through the use of finite-element analysis, is also presented. The inputs that are required for the discrete cohesive zone model (DCZM) are identified. Compact tension specimen fracture tests and double notched tension tests were carried out to measure the fracture energy ( $G_{Ic}$ ), and the maximum cohesive strength ( $\sigma_c$ ), of the 2DTBC. The DCZM modeling strategy was independently verified by conducting single edge notched three-point bend tests using a modified three-point bend test fixture. The experimental and numerical analyses were carried out for two different types of 2DTBC made from the same textile architecture but infused with two different resin systems to validate the proposed methodology.

## Introduction

Textile fiber composites are finding increased use as a structural material in a variety of aerospace and automotive

industrial applications. An appealing property of such composites is their high specific energy absorption capability under compressive crush loads [1]. Due to the high degree of interweaving of fiber tows in the material microstructure, damage accumulation through distributed micro-cracking of the matrix is preferred over the coalescence and growth of macroscopic cracks; the microstructure presents “obstacles” to the propagation of a macroscopic crack, leading to a mechanism that produces enhanced toughness. Stiffer and tougher materials can be designed with textile composites by suitably tailoring the design of the textile tows [2], with the choice of an appropriate polymer matrix. The replacement of metal structural parts by equivalent composite structural parts can lead to weight savings that translate to reduced operational costs of a vehicle, an attribute that appears to be necessary for the success of future anticipated automobiles powered by alternative energy sources [3].

The requirement to demonstrate structural integrity and damage tolerance necessitates a fundamental understanding of the mechanical response, damage tolerance, and damage growth of a load bearing composite structure [4]. While a fairly substantial literature is present on addressing damage growth in the form of delamination crack growth, lying parallel to the interfaces of the different layers of a composite, much less is known or understood about damage propagation when a crack or damage in the form of a crack is present through the thickness of a composite structure. The influence of such a crack on the load bearing ability of a homogeneous and isotropic material has received considerable attention in the past; however, a similar effort at resolving issues in a non-homogeneous and macroscopically orthotropic structure is still a problem that requires resolution [5]. Because of the different length scales associated with the microstructure of a composite material and the

---

A. G. Salvi · A. M. Waas (✉)  
Department of Aerospace Engineering, University of Michigan,  
Ann Arbor, MI 48109-2140, USA  
e-mail: dcw@umich.edu

A. Caliskan  
Vehicle Design and R&A Department, Ford Motor Company,  
Dearborn, MI 48121, USA

resulting composite structure, a multitude of failure mechanisms can operate simultaneously, leading to a very complex picture associated with the manner in which damage progresses in a composite structure. Even though a sharp (crack tip radius much smaller than the other characteristic dimension) through the thickness crack can be present in a composite structure, as soon as damage (this can be in the form of matrix micro-cracking) accumulates at the crack tip, crack blunting and spreading of such damage (this can involve tow separation and ply delamination, in addition to matrix cracking) in the highly stressed areas around this initial crack occurs. When this initial damage zone starts to grow, a zone of material that is considerably larger than that would be found in a monolithic material, in the form of a band, is seen to grow along with this crack-like feature. That is, there is no clean “crack” that can be identified as in a monolithic material like metal. Instead, a diffused zone of damage is seen to advance. A large toughness is associated with this damage growth, largely influenced by the tows that bridge the damage zone, providing additional resistance for primary crack growth. This additional resistance is very desirable and is a major contributor to the increased toughness of 2D triaxially braided carbon fiber textile composites (2DTBC). Currently, for aerospace applications, a factor of safety (FS) of 1.4 is used for metallic structures whereas an FS of about 2.0 is used for fiber-reinforced composite structures. This disparity in FS can be alleviated by developing robust, mechanics-based predictive models of composite behavior. The discrete cohesive zone model (DCZM) methodology that is proposed in this paper is aimed at advancing such a goal.

Linear elastic fracture mechanics (LEFM) has been developed and implemented within FE codes to study a variety of fracture problems. Essential to the success of LEFM approaches is the requirement of a small process zone ahead of the crack tip [6]. Depending on the size of this process zone, LEFM ideas can be extended to include plasticity dominated effects, but beyond a certain size of this process zone, other modeling strategies, such as the cohesive zone modeling approach, have found favor in a wide variety of fracture problems. Among fracture parameters, the strain energy release rate is used increasingly in conjunction with LEFM. It can be computed by the virtual crack closure technique (VCCT) [7], in conjunction with FE analysis. The application of VCCT is predicated on the requirement of a pre-existing crack with a sharp and neat tip within a material for crack initiation and conditions of small-scale yielding to hold. With negligible material non-linearity at the crack tip (small process zone size), LEFM-based approaches have been proven to be effective in predicting crack initiation and subsequent growth [6–11].

In many cases of crack growth in composite materials and structures made of other quasi-brittle materials, the

process zone size may be larger than any characteristic length scale in the problem leading to situations where the basic tenets of LEFM cease to hold [12]. Several mechanisms can contribute to this situation. Micro-cracking, fiber bridging, coalescence of voids, and other mechanisms at the microstructural scale can give rise to a process zone that is considerably larger than what is required for assumptions of LEFM to hold. A new length scale,  $l^*$ , emerges that is related to a characteristic elastic modulus  $E$ , fracture toughness  $G_{IC}$  and cohesive strength,  $\sigma_c$ , defined as  $l^* = EG_{IC}/\sigma_c^2$ . If  $l^*$  is larger than any characteristic length scale in the problem, then cohesive zone models (CZM) become an indispensable tool for analysis [13–18]. The origin of the CZM can be traced back to the Barenblatt–Dugdale (BD) model that was introduced for fracture in ductile metals, with the concept that stress within the zone ahead of the crack tip is limited by the material yield strength and thus generates a plastic strip of constant stress ahead of the intended crack path [6]. The CZM assumes that a cohesive damage zone (in this zone stress can decrease with increasing opening and/or shearing) develops ahead of the crack path without necessarily requiring that the stress be constant within this zone. Therefore, the CZM is a broader generalization of the BD model.

In order to implement a CZM in its simplest form, two parameters are required: a fracture toughness (or energy) and a cohesive strength. The choice of these parameters and how they are measured and/or calibrated depends on the problem that is being addressed. In general, the CZM parameters are “system” parameters and are related to the material system that is being studied. The fracture toughness can be obtained from coupon level tests of the material system under study. This measured toughness value in conjunction with a CZM/FE simulation of the test can be used to back out the cohesive strength. Alternatively, both the toughness and strength can be measured from coupon level tests for subsequent use in prediction of crack growth in other structural configurations. In the CZM, an existing crack starts to grow when the stress at the crack tip attains the cohesive strength *and* when there is sufficient energy supplied from the system to create new cracked area associated with the advancing crack. Thus, unlike LEFM, which requires one parameter, a CZM strategy requires two parameters for predicting crack growth. A cohesive law combines fracture energy and cohesive strength to describe the resistance offered to crack advancement within the cohesive zone. Various postulated forms of cohesive laws (such as triangular, exponential, trapezoidal, multi-section, etc.) have been attempted in conjunction with CZM [19–23]. These studies have shown that the form of the phenomenological cohesive law is less important than the well-posed implementation when CZMs are used with FE analysis. Recent studies [24] have adopted a Kriging

analysis method to investigate the sensitivities of the CZM parameter.

This paper is concerned with the development of a procedure by which damage growth in the form of a crack-like zone, emanating from an initial crack-like flaw, in heterogeneous and orthotropic materials can be characterized. In addition to characterizing the 2DTBC as an orthotropic elastic (or elastic–plastic) medium, additional parameters that are necessary for implementing a DCZM [10–12] are identified and quantified. The procedure is validated by performing independent experimental measurements on a single-edge notch three-point bend (SETB) configuration and using the DCZM to predict the response of the SETB tests during crack growth.

The proposed method is further validated by carrying out the same procedure on 2DTBC made from two different matrix materials. A vinyl ester Ashland Hetron 922 and Epon 862 epoxy are used to produce two different types of 2DTBC, for the studies reported here.

### Compact tension specimen fracture tests on 2DTBC

#### Specimen architecture of 2DTBC

Figure 1 shows the architecture of a  $0/\pm 45^\circ$  2DTBC used in the present study. Eight braided composite fiber mats (axial tows consisting of 80,000 fibers and biased tows consisting of 12,000 fibers with fiber volume fractions of 55% and 52% for Hetron and Epon, respectively) were stacked together and matrix is then infused. Two types of composites were prepared by using two different resin systems, but with the same fiber tow architecture. Ashland Hetron 922 vinyl-ester and Epon 862 epoxy resin were used as resins for these composites. It was speculated that energy absorption due to fracture in 2DTBC is sensitive to

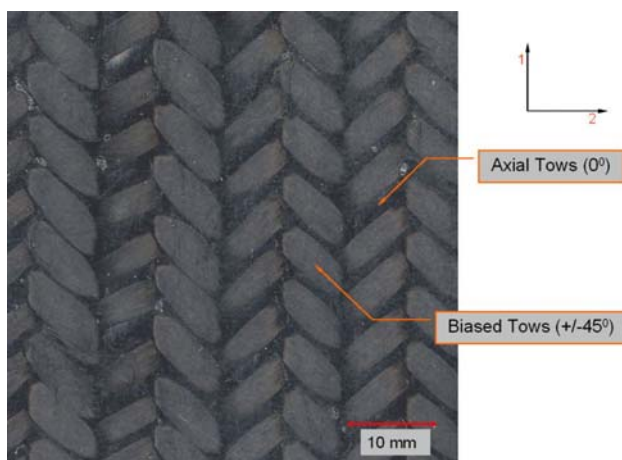


**Fig. 1** Architecture of 2DTBC

**Table 1** Material properties for 2DTBC Hetron and Epon specimens

Material properties	Hetron (GPa)	Epon (GPa)
$E_{11}$	$68.5 \pm 6.1$	$105.0 \pm 9.0$
$E_{22}$	$10.9 \pm 1.4$	$15.2 \pm 0.8$
$G_{12}$	$7.5 \pm 1.4$	$11.5 \pm 1.7$
$\nu_{12}$	0.36	0.34

fiber–matrix interface, fiber wetting, and in general the quality (voids) of the composite. This was one of the reasons why two different resin systems were used to prepare 2DTBC with the same fiber tow architecture. The tensile modulus in the manufacturer’s specification for the virgin Hetron and Epon resin is given as, 3.17 and 3.24 GPa, respectively.

The 2DTBC is modeled as a homogenous orthotropic elastic–plastic material for the modeling studies. The four principal material elastic properties, denoted as  $E_{11}$ ,  $E_{22}$ ,  $\nu_{12}$ , and  $G_{12}$ , were measured by using American Society for Testing and Materials-specified standard material property tests. Dog bone-shaped specimens were used to measure elastic moduli ( $E_{11}$  and  $E_{22}$ ) and Poisson’s ratio ( $\nu_{12}$ ), and, the Iosipescu shear test was performed to obtain the shear modulus ( $G_{12}$ ). Table 1 summarizes the effective elastic mechanical properties of Epon and Hetron specimens. It was observed that, even though the virgin matrix properties are very similar, the composite properties for Epon and Hetron are significantly different. The reasons for these findings are discussed in this paper.

#### Experimental procedure for CTS tests

Compact tension specimen (CTS) fracture tests were carried out to measure the fracture energy of these composites. CTS specimens, 3 in.  $\times$  4.5 in. (76.2 mm  $\times$  114.3 mm), were cut using a water jet and a 2-in. (50.4 mm) long notch was introduced as shown in Fig. 2a. A sharp knife-edge was used to introduce an initial crack as shown in Fig. 2b. The specimens are made up of eight layers of braided mats. When seen under the microscope it was observed that they do not stack up in-phase, i.e., all the axial tows do not line up one on top of another. So when a notch is cut in the specimen, it cuts through axial tows, biased tows as well through the matrix pockets in between the tows in different layers of the same specimen. It was observed that this does not affect the results since the notch placement was varied with respect to the position of the axial tows, and it was found that the crack growth behavior and the  $P$ – $\Delta$  response was indistinguishable amongst specimens.

The load was applied through pins as shown in Fig. 2c. Load ( $P$ ) and load-point displacement ( $\Delta$ ) were measured during the experiment. Crack initiation and propagation, as

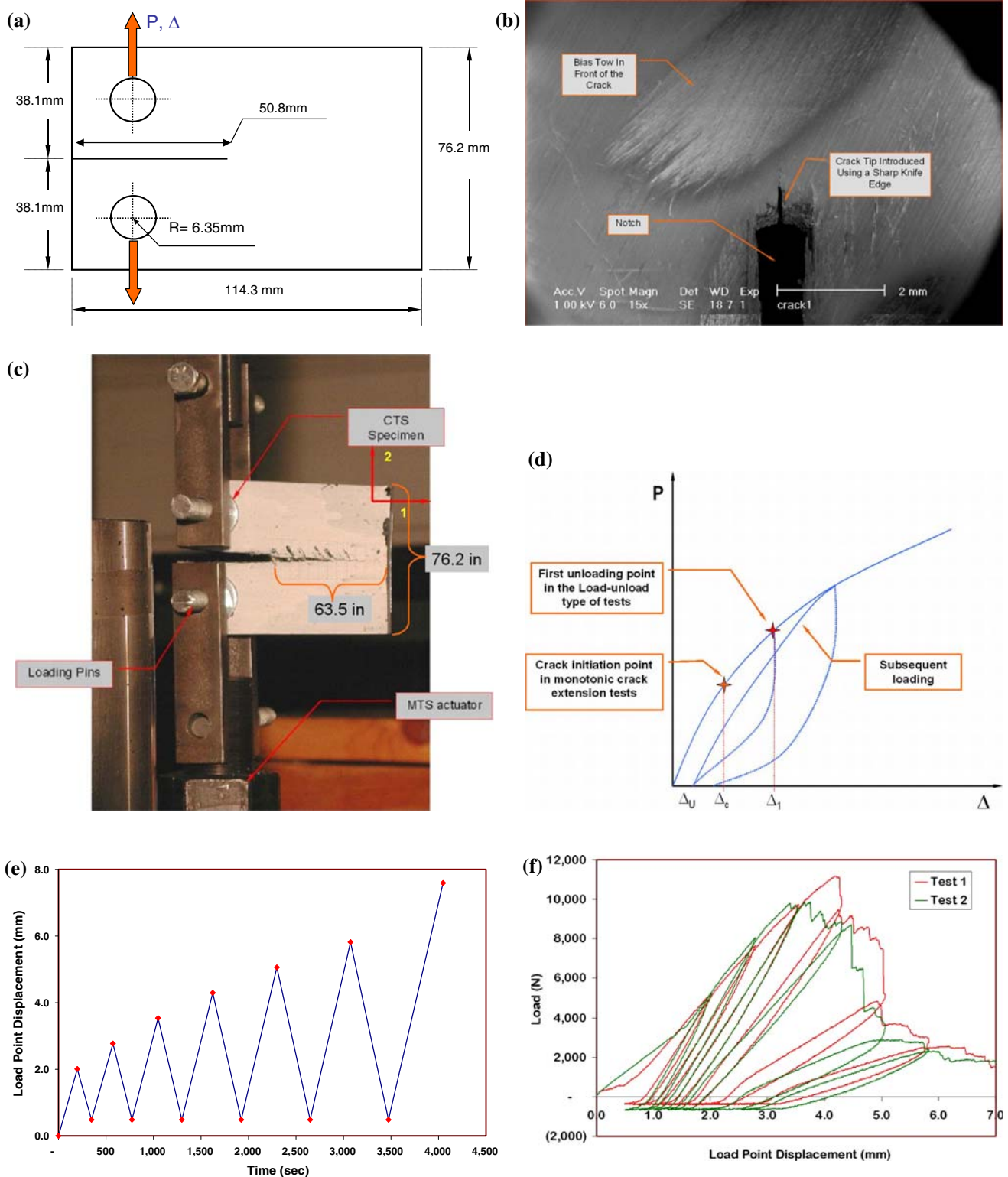


**Fig. 2** (a) CTS configuration. (b) SEM image of crack tip in a Hetron 2DTBC. (c) CTS experimental set-up. (d) Loading cycle in a typical cyclic fracture test. (e) Applied load-point displacement as a function of time. (f)  $P$  versus  $\Delta$  behavior for cyclic CTS fracture test (Hetron)

indicated on the specimen surface, were captured using a Kodak high-resolution digital camera. In selected specimens, both lateral surfaces were imaged to ascertain that

there are no significant through the thickness variation in the crack position. Specimens were loaded on a hydraulically activated MTS machine at a rate of 0.0004 in./s

(0.01 mm/s). Experiments were carried out on both Epon and Hetron 2DTBC. On the lateral surfaces of the specimen, scribe marks,  $\approx 0.1$ -mm deep, were placed along the intended crack path.

Two types of loading patterns were used to load the specimens. In the first set of tests, specimens were loaded monotonically until failure. In the second set of tests, the specimens were loaded and unloaded cyclically in a controlled manner so that the “primary crack” grows in each of the cycle. This was done so that the elastic energy associated with the fracture can be separated (by unloading the specimens) from the total fracture energy. In cyclic loading, a specific loading pattern was adopted. Information from the initial monotonically loaded fracture specimens was used to determine the primary crack initiation load and the corresponding load-point displacement ( $\Delta_c$ ) as shown in Fig. 2d. Subsequently, specimens were loaded beyond  $\Delta_c$  to  $\Delta_1$ , to initiate and extend the primary crack. Specimens were then unloaded to a certain point  $\Delta_U$  where the load drops to zero. Once  $\Delta_U$  is reached, the specimen is again loaded up to  $\Delta_2$  and unloaded to  $\Delta_U$ . This cycle is repeated several times as shown in Fig. 2d. Figure 2e shows the applied displacement as a function of time. Figure 2f shows a typical load versus load-point displacement behavior for two cyclic loading tests (T1 and T2) for Hetron specimens.

#### Experimental observations

Figure 3a shows typical load ( $P$ ) versus load-point displacement ( $\Delta$ ) behavior of a monotonically loaded Hetron specimen and Fig. 3b shows the load versus load-point displacement behavior for a typical Epon specimen. Note that symbol “H” in the figure legends refers to Hetron specimens while the symbol “E” in the figure legends refers to Epon specimens. In the cyclic tests, the crack propagation during loading was captured by a high-resolution digital camera. Figure 3c shows an image of crack opening during the CTS fracture tests. Crack extension during each loading cycle was measured. The primary crack grows in spurts with each spurt arrested by the biased braids that are at angle of  $45^\circ$  to the direction of crack path. Extensive damage is associated with the advancing primary crack. Because the state of stress surrounding the crack-like region is expected to be elevated compared to the areas remote from the crack front, the damage region surrounding the advancing crack is diffused and there is a large region of bridging that develops as the specimen is continued to load. What is remarkable is the “path independency” that is displayed by these specimens. For a given load-point displacement ( $\Delta$ ), the values of applied load that are required to attain such a displacement are indistinguishable between the cyclic tests and the monotonically loaded tests. However, the cyclic tests reveal a

considerable amount of hysteresis. This is because the unloading cycle does not bring the state of material surrounding the crack tip back to what it was prior to loading, indicative of the energy dissipation that occurs at the crack tip, leading to the hysteresis.

In the monotonically loaded tests, as the initial crack advances, it forms a bridging zone as shown in Fig. 3d. This bridging zone consists of biased braids that are at  $45^\circ$  to the direction of (axial tows) crack propagation. As the crack progresses, the bridging zone increases in size. However, once a critical length of the bridging zone is formed, it stays approximately constant and travels with the advancing crack-like zone. Once this bridging zone approaches the vicinity of the load application point, it starts to fail (biased braids) thus leading to a drop in the overall load. As the crack bridging diminishes, due to unstable crack growth in the specimen, the overall load drops sharply (refer to Fig. 3a). Figure 3e shows an image of crack opening and bridging zone formation. Figure 3f shows an actual image sequence of the bridging zone formation and bridging zone translation as viewed on the surface of the specimen. Figure 4a, b shows the primary crack tip positions at the end of each load–unload cycle for Hetron and Epon specimens, respectively. The crack initiation and progression differs somewhat, as the microstructure for each specimen is different. The initial crack position with respect to the braid architecture is not exactly the same for different specimens.

Fracture energy was measured by calculating the area under each loading–unloading curve, which represents the energy lost in fracture of the specimen or the crack propagation during that cycle [25]. For each test, the area enclosed within each loop of the  $P$ – $\Delta$  response was calculated. The local dissipated energy per cycle is obtained as,

$$G_{Ic} = \frac{\text{Area}(P\Delta)_i}{2C_i t}, \quad (1)$$

where, area  $(P\Delta)_i$  = area under  $i$ th loop,  $C_i$  = crack extension during  $i$ th loading,  $t$  = thickness of the specimen. Note that even though the specimens tested in this study exhibited crack growth locally in multiple modes, and along multiple planes, some of which were oriented at off-axis angles, here we use the symbol  $G_{Ic}$  to represent the fracture energy because on the macroscopic scale a “crack-like” feature grows under mode I conditions.

Figure 4c, d shows the fracture energy ( $G_{Ic}$ ) as a function of “primary crack” position. It can be observed that the fracture energy as a function of crack position is not smooth and non-uniform for each specimen. However, an examination of the results from the monotonic tests shed more light on the observed test data from the cyclic tests.

In the monotonically loaded specimens, the crack position was measured during the entire envelope of the

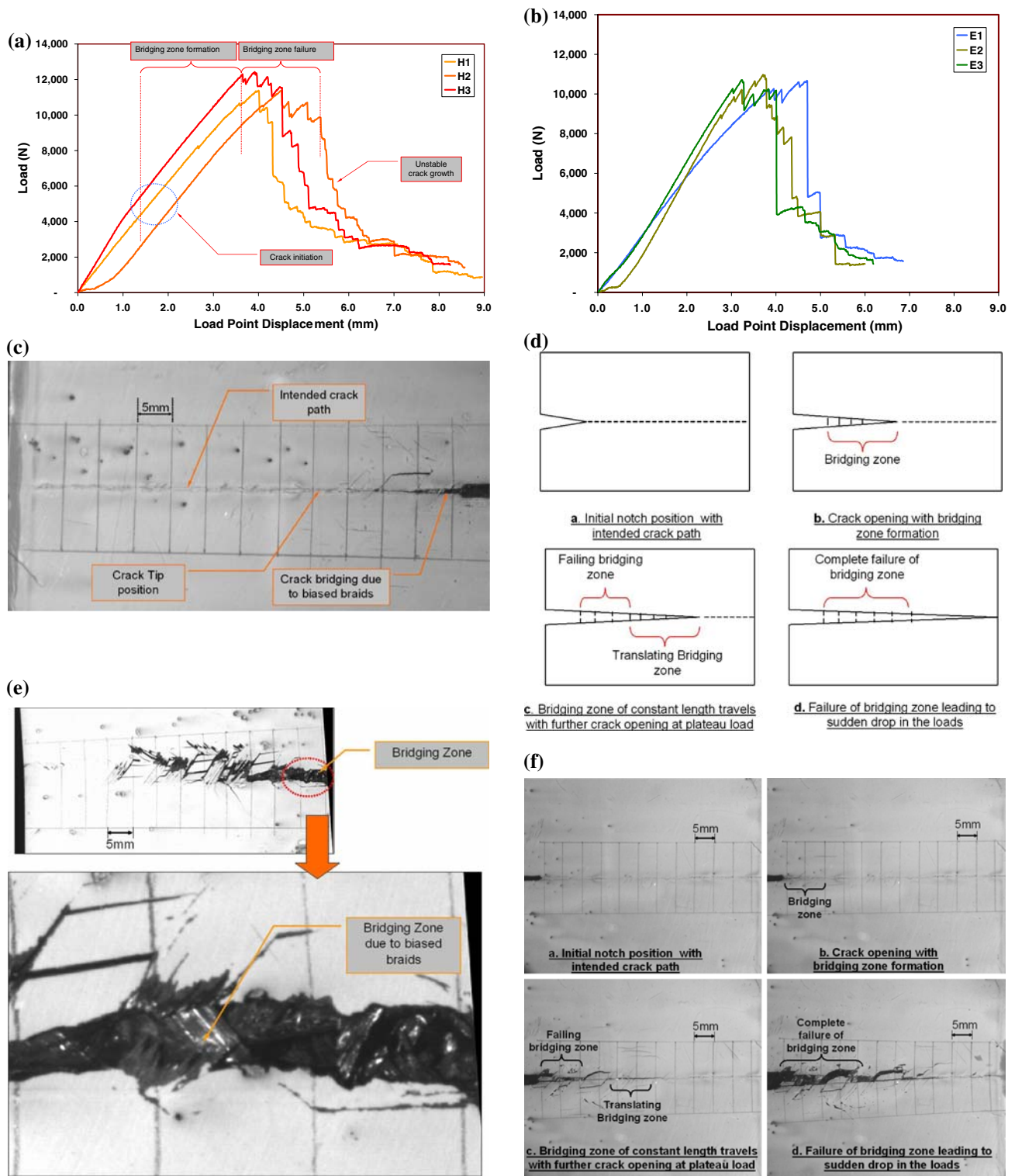


**Fig. 3** (a)  $P$  versus  $\Delta$  behavior for monotonic CTS fracture tests on Hetron specimens. (b)  $P$  versus  $\Delta$  behavior for monotonic CTS fracture tests on Epon specimens. (c) Bridging zone formation and

failure. (d) Formation and translation of bridging zone. (e) Formation of crack opening and bridging zone. (f) Formation and translation of bridging zone

loading. Figure 4e, f shows the crack position versus time for the monotonically loaded Hetron and Epon specimens, respectively, while Fig. 4g shows the behavior of specimen

compliance versus time for these tests. It was observed that the compliance is almost constant initially. As the crack grows, the specimen becomes more compliant due to the

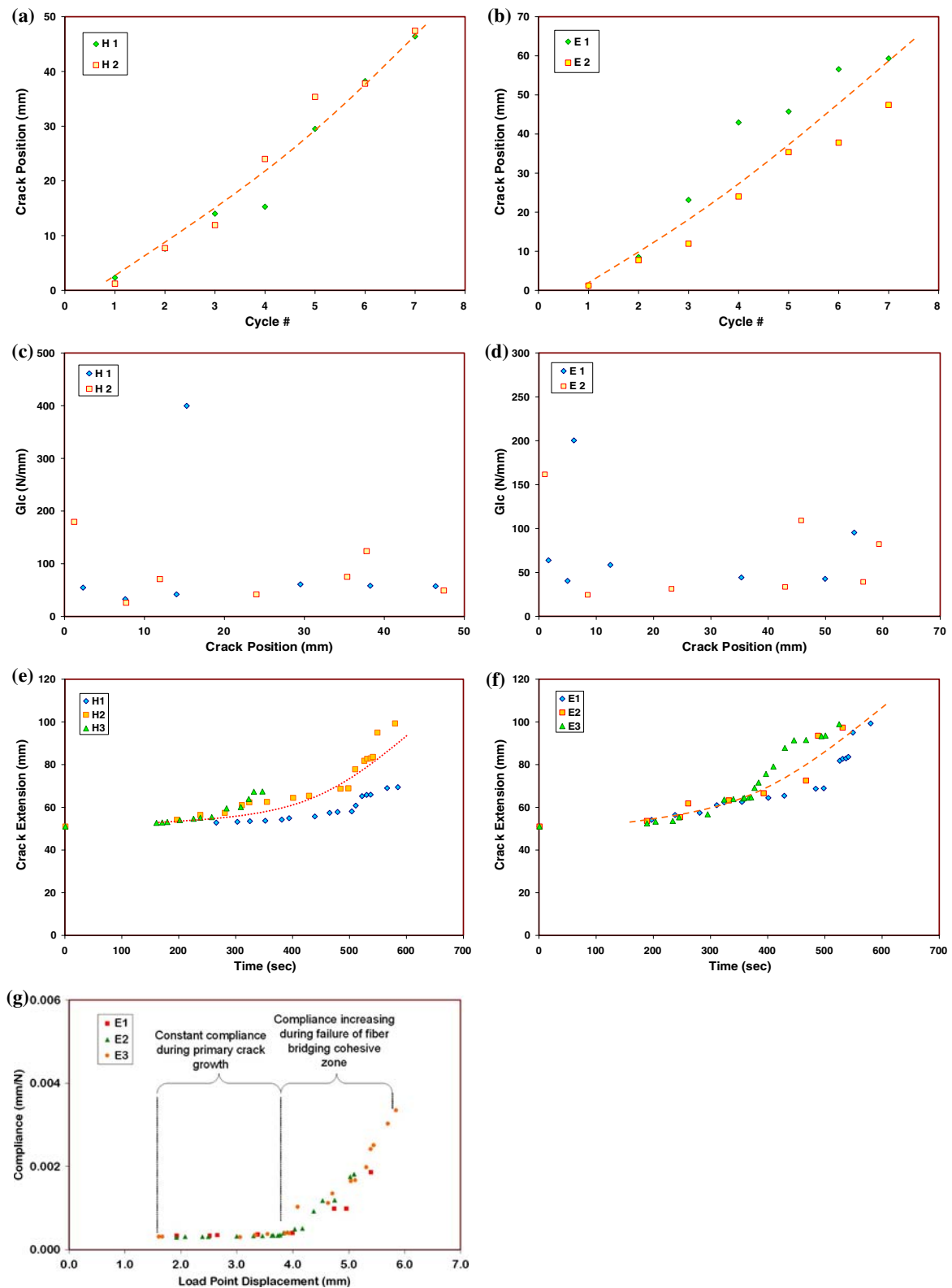


**Fig. 4** (a) Crack extension versus time for Hetron specimens. (b) Crack extension versus time for Epon specimens. (c) Fracture energy as a function of crack extension For Hetron. (d) Fracture energy as a function of crack extension For Epon. (e) Crack extension versus time

for monotonic fracture tests on Hetron. (f) Crack extension versus time for monotonic fracture tests on Epon. (g) Compliance versus time for Hetron specimens

failure of the fiber-bridging zone, which diminishes the resistance to further crack advance (post-peak load behavior).

The data from the monotonic tests was analyzed as follows. The entire crack length was used to obtain averaged fracture energy for advancing the crack by the entire crack growth length. This energy is calculated by considering the entire area under the work input curve ( $P-\Delta$  curve). This method of obtaining an “averaged” fracture energy is more suitable for this class of non-homogenous materials that involve a number of competing and complex mechanisms that contribute to the overall fracture energy.

Experimental procedure for double-notched tension tests

The value of cohesive strength ( $\sigma_c$ ) that is to be used in the cohesive law of the DCZM can be related to the transverse strength of the composite (the strength in a direction that is normal to the crack advancement direction). Braided specimens, 2 in.  $\times$  7 in. (50.8 mm  $\times$  177.8 mm) long, were cut and a notch of 0.5 in. (12.7 mm) was introduced on both the edges, in the center of the specimen as shown in Fig. 5. The specimens were loaded in tension in the direction perpendicular to the direction of the axial tows. The axial stress, based on the net section area, and load-point displacements were measured in the experiment. The average transverse strength ( $\sigma_c$ ) of the Hetron composite was  $\approx 66 \text{ N/mm}^2 (\pm 3 \text{ N/mm}^2)$ . Using the measured values of transverse strength  $\sigma_c$ , and fracture energy,  $G_{Ic}$ , a full description of the DCZM cohesive law can be obtained. The average transverse strength ( $\sigma_c$ ) of the Epon composites was found to be  $62 \text{ N/mm}^2 (\pm 3 \text{ N/mm}^2)$ . Five tests were performed to obtain the averaged values and deviations in  $\sigma_c$ . The notch geometry was selected such that the net section was at least 4 unit cells (this is the periodic representative volume element of this textile composite) wide. With that in mind, the width of the specimen was selected so that the failure will occur in the net section.

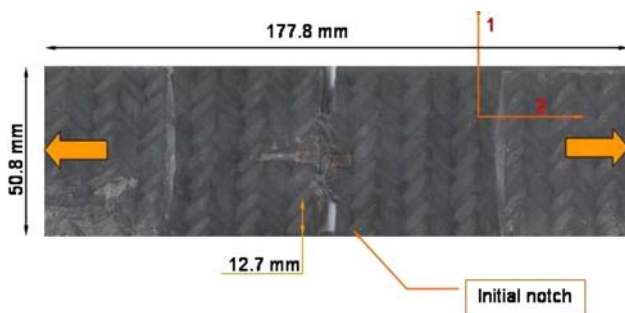


Fig. 5 Tension specimen to investigate the transverse fiber tow strength

Discrete cohesive zone model

A DCZM was developed [10, 12], which simulates the fracture of CTS configuration. The central idea of DCZM is to treat material separation as being represented by a discrete bed of springs that communicate between opposite node pairs on the faces of material that needs to be decohered. A non-linear “spring-type” discrete 1D element is placed between interfacial node pairs to model cohesive interactions between surfaces along the crack path as shown in Fig. 6a. The numbers 1–4 are the node numbers along the crack faces as indicated in the figure. The dashed line indicates the node numbers that are being used in implementing the DCZM. The traction separation law is enforced between nodes 1 and 2, while the “dummy” nodes 3 and 4 are used to calculate the orientation of the crack face. In this paper the orientation is not significant but in more general problems with large deformation (non-linear geometry) instantaneous crack path orientation can be important. More details of the DCZM are given in [12].

The 2DTBC is treated as an elastic–plastic orthotropic homogenized material for modeling. The plasticity of the specimen is described using a one-parameter plasticity model (see Appendix). The fracture tests were simulated by using the DCZM-based interface elements which were implemented into ABAQUS® by using a user element subroutine UEL.

In this paper, a triangular cohesive law is used as shown in Fig. 6b. Based on the energy required to advance the primary crack, we have,

$$\frac{1}{2} \sigma_c \Delta_m = G_{Ic}, \tag{2}$$

where  $G_{Ic}$  is the fracture energy of the material that is to be measured through the CTS tests.  $\delta_m$  and  $\sigma_c$  are the maximum nodal opening and the critical cohesive stress, respectively. In this study, we choose  $\sigma_c$  as the cohesive parameter. The numerical value of cohesive stress ( $\sigma_c$ ) is set by carrying out tension tests on notched dog-bone specimens, as presented earlier, and  $\delta_m$  is then calculated from Eq. 2, so that  $G_{Ic}$  is preserved. The critical value for the cohesive force in the DCZM element is

$$F_c = \sigma_c B \Delta a = \frac{2G_{Ic} B \Delta a}{\delta_m}, \tag{3}$$

where,  $B$  is the out-of-plane thickness of the specimen and  $\Delta a$  is the difference between initial notch tip and crack tip position. Since the spacing of the DCZM element depends on the coordinates of the nodes,  $F_c$  depends on the mesh size (note  $\sigma_c$  is independent of element spacing). The critical opening ( $\delta_c$ ) is calculated by

$$\delta_c = \frac{F_c}{K_y}, \tag{4}$$



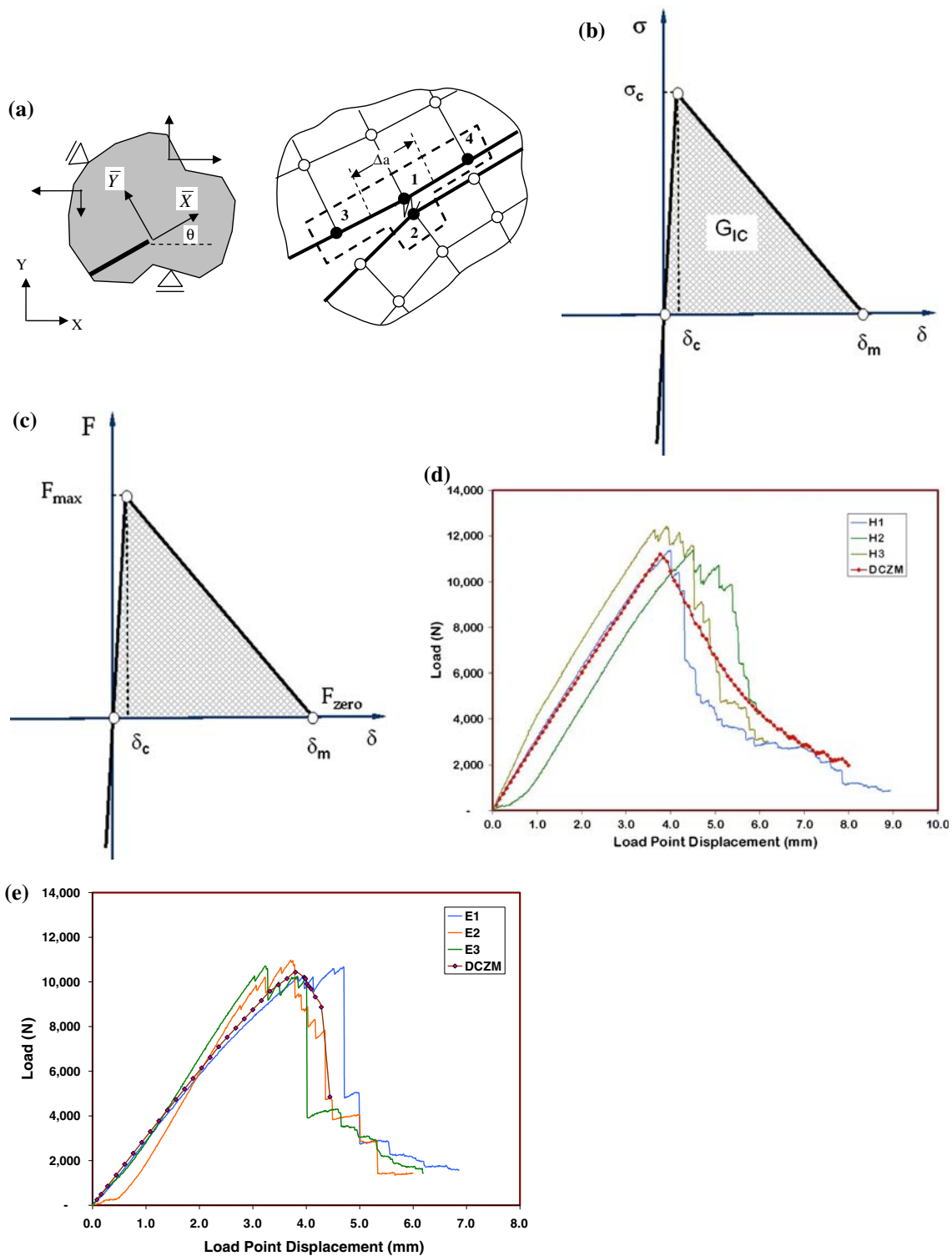


**Fig. 6** (a) Interface element for slant crack lying in  $(X, Y)$  plane. (b) Triangle type cohesive law used in DCZM. (c) Spring law used for cohesive elements in DCZM. (d) DCZM prediction for Hetron CTS specimens. (e) DCZM prediction for Epon CTS specimens

where  $K_{\bar{y}}$  is the initial stiffness of the DCZM element which is selected to be a very high value relative to the stiffness of the bridged material. Figure 6c shows the force–displacement ( $F$ – $\delta$ ) spring law thus obtained from Eq. 3.

In order to apply the triangular cohesive law, when  $\delta \leq \delta_c$ ,  $K_{\bar{y}}$  is set to be a very large to ensure that the crack is initially closed. In numerical implementation, this value usually is chosen to be three orders of magnitude larger

than the major Young’s modulus of the specimen. When  $\delta_c < \delta < \delta_m$ , the softening part of the cohesive zone,  $K_{\bar{y}}$  is determined as

$$K_{\bar{y}} = -\frac{F_c}{\delta_m - \delta_c} \quad (5)$$

Finally, when  $\delta \geq \delta_m$ , the DCZM element fails completely, and  $K_{\bar{y}} = 0$ . A constant fracture energy ( $G_{Ic}$ ) value of 57 N/mm was used to simulate the CTS fracture tests for Hetron specimens. Figure 6d shows the comparison of experimental and DCZM simulation of  $P-\Delta$  response. Similarly, constant fracture energy ( $G_{Ic}$ ) value of 41 N/mm was used to simulate the CTS fracture tests for Epon specimens and the  $P-\Delta$  behavior is shown in Fig. 6e. The calibration of the DCZM parameters in the manner provides confidence for its predictive capability for other general damage growth configuration.

**SETB fracture tests: validation of the proposed scheme**

**Experimental procedure**

In order to validate the proposed DCZM, calibrated in conjunction with the CTS tests and the double-notched tension tests, an independent set of fracture tests was carried out using an SETB specimen. Figure 7a shows the configuration and dimensions of the specimen. Hetron and Epon specimens were monotonically loaded on a hydraulically activated MTS machine. The specimen was secured on top of two steel rollers and loaded using a top-loading pin attached to the crosshead of an MTS servo hydraulic loading frame at a displacement rate of 0.01 mm/s. A high-resolution (7.5 Mega pixel) camera was used to take images at 1-s intervals to keep track of the crack trajectory during the loading history. The applied load was measured using a load cell attached to the MTS test frame and the load-point displacement was measured using an LVDT. Figure 7b shows the test set-up for SETB fracture tests.

**Experimental observations**

The  $P-\Delta$  behavior for the Hetron and Epon specimens was measured. Also the crack tip positions during the monotonic loading for both Hetron and Epon specimens were measured by analyzing the images taken during the entire loading envelope. Similar to the monotonic CTS fracture tests, the fracture energy was calculated by measuring crack length and the area under the  $P-\Delta$  curve.

It was observed that the smaller fracture energy ( $G_{Ic}$ ) value of Epon specimen is indicative of the reduced energy absorption performance when compared to Hetron specimens, i.e., in the post-peak load regime, the Hetron

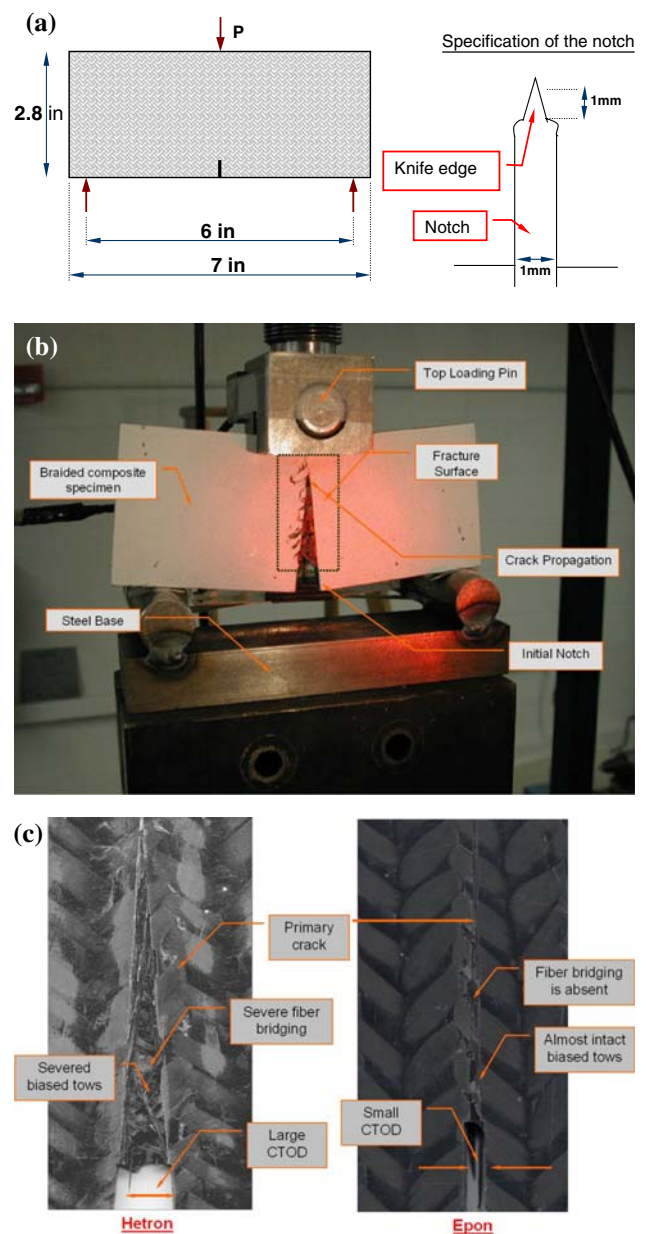


**Fig. 7** (a) Dimensions of the test specimen and loading configuration. (b) SENB fracture test fixture. (c) Extent of damage in Hetron and Epon specimens

specimens absorb more energy than Epon specimens. Upon close inspection of the specimens, it was found that the Hetron specimens show a larger damage zone than that of the Epon specimens as shown in Fig. 7c. The extensions within the bridging zone are much larger in the Hetron samples leading to larger crack opening displacements. As the primary crack grows in the specimens, the energy is dissipated by matrix cracking, breaking of the fiber bridging tows, and fiber matrix separation. Hetron specimens show larger amounts of fiber bridging, and a large amount of secondary cracking in the vicinity of the primary

crack. Epon specimens show very little fiber bridging and almost negligible diffused cracking in the fiber tows that bridge the crack. Also, in the Epon specimens, the area adjacent to the primary crack shows very little matrix damage. These observations are reflected in the measurements that indicate Hetron 2DTBC to be a better energy absorber than Epon 2DTBC.

#### DCZM for SETB tests

A DCZM for the SETB configuration was developed to validate the usefulness of the DCZM. A fracture energy value of 57 N/mm, which was obtained from the CTS simulation in conjunction with the CTS tests, was used for the SETB simulation. The SETB model was created with three mesh densities: case A = 1,610 elements, case B = 6,570 elements, and case C = 2,6280 elements as shown in Fig. 8a. Figure 8b shows the prediction of the DCZM for SETB fracture tests for Hetron specimens. The

DCZM predictions are very close to the experimental results. The DCZM model was modified to include plasticity of the 2DTBC by writing a UMAT subroutine that models the 2DTBC through a one-parameter plasticity model. The plasticity parameter  $a_{66}$  was measured by carrying out off-axis compression tests [12, 26, 27].  $a_{66}$  for Hetron specimens was found to be 1.2. Results obtained with the inclusion of plasticity are shown in Fig. 8c. It was found that including plasticity improved the results for the  $P$ - $\Delta$  prediction between experiment and simulation. A similar DCZM was developed for Epon specimens. Previously measured material elastic properties of Epon specimens were used along with a fracture energy value of 41 N/mm, cohesive strength of 62 N/mm<sup>2</sup>, and plasticity parameter  $a_{66} = 1.1$ . Figure 8d shows the comparison of DCZM predictions with experimental results. All the calculations were carried out using the finest mesh. It was observed that the DCZM predictions agree well with the test data. Figure 8e, f shows the images taken at certain

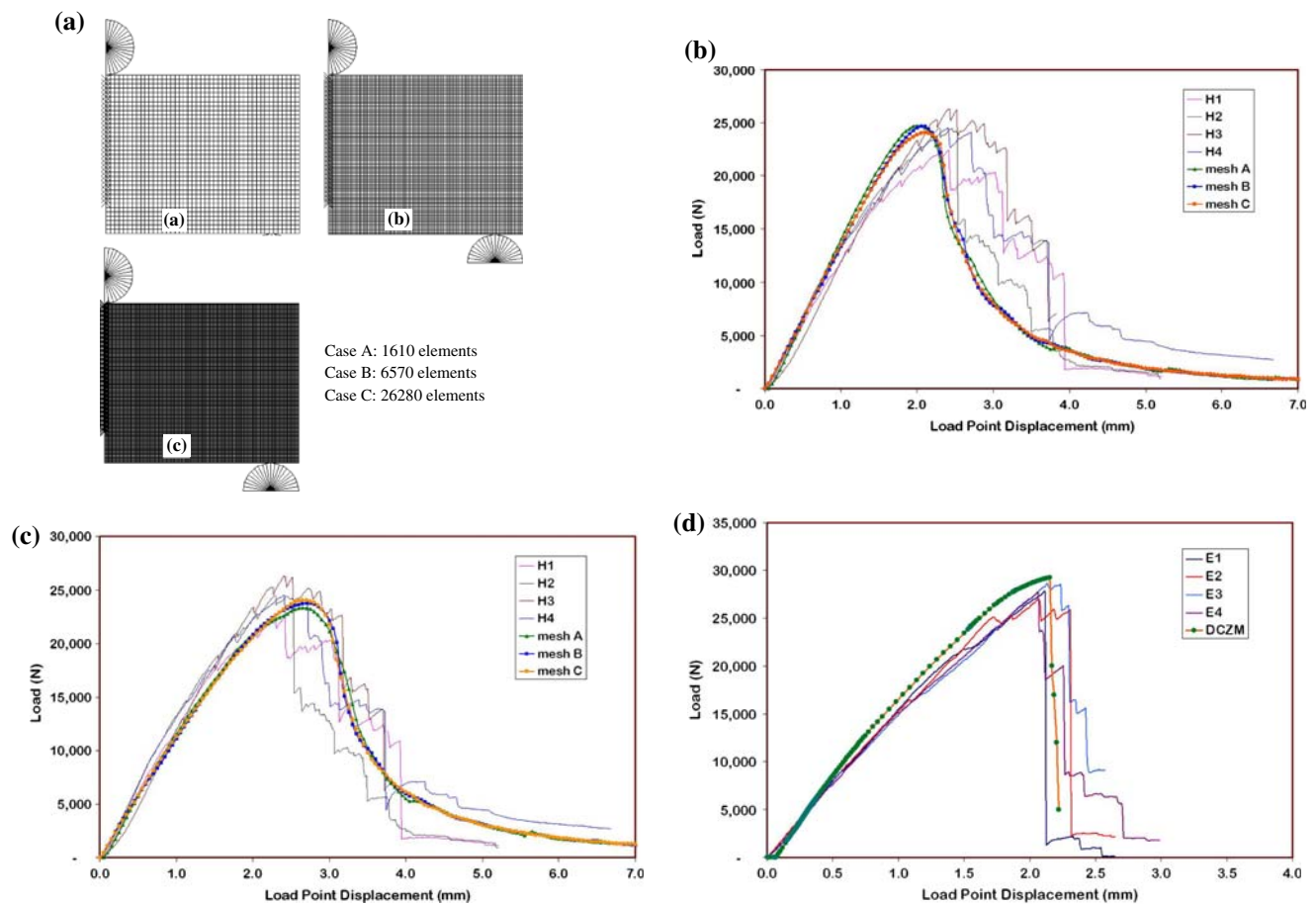


**Fig. 8** (a) Three FEA meshes with different element density. (b) Comparison between experiments and DCZM. (c) Comparison between experiments and DCZM with inclusion of plasticity for Hetron. (d) Comparison between experiments and DCZM with

inclusion of plasticity for Epon. (e) Sequence of images taken during the SENB fracture test. (f) Sequence of DCZM simulations during the SENB fracture test. (g) Comparison of crack position in experiment and DCZM. (h) Location of bridging zone in DCZM simulation

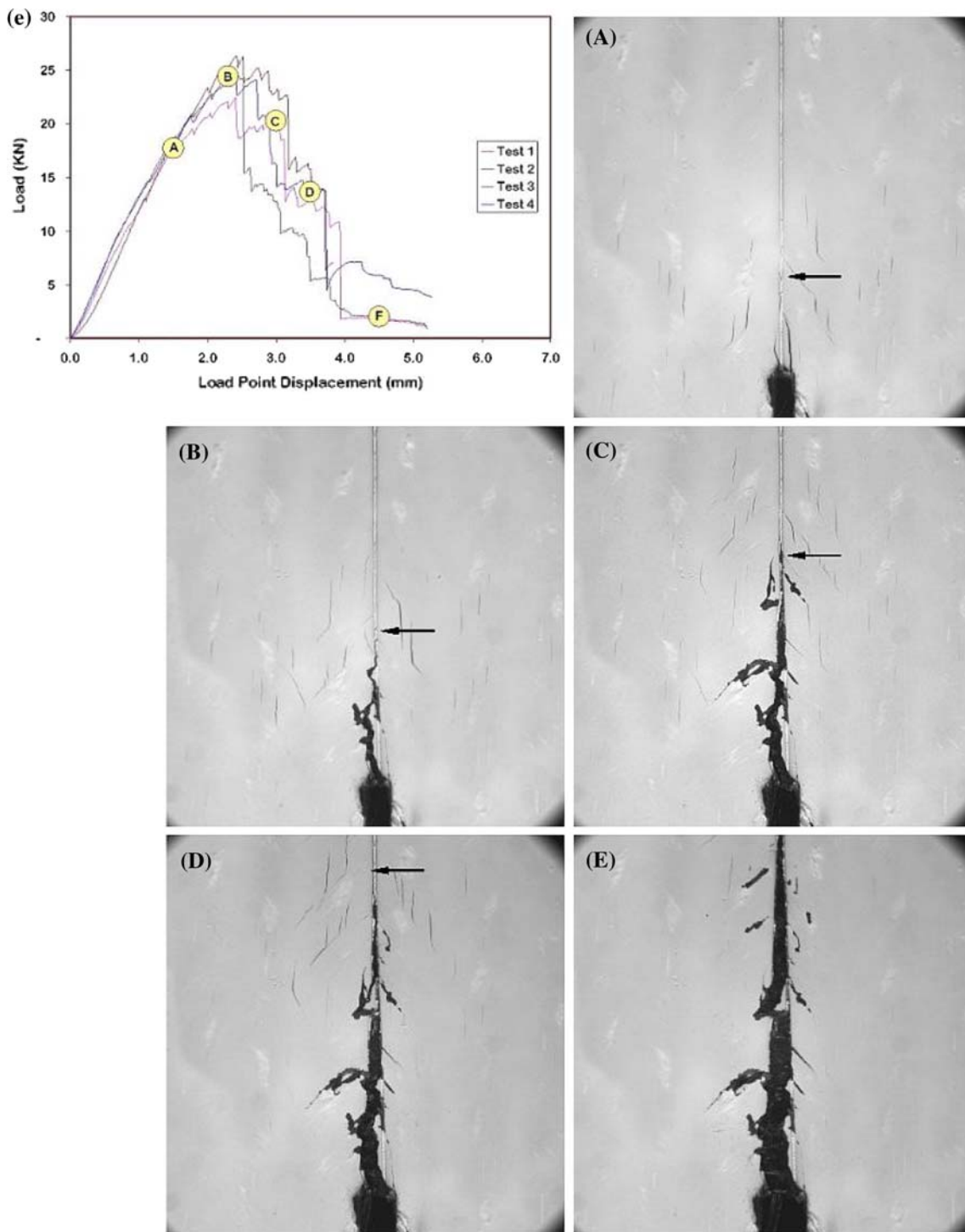


Fig. 8 continued

intervals during experiment and DCZM simulation. In the DCZM simulation, the cohesive force in each element was tracked. The location of the element corresponding to maximum force ( $F_{max}$  in triangular cohesive law for fracture) and minimum force ( $F_{zero}$ ) (refer Fig. 6c) was plotted

against the surface crack tip measured in the experiment as shown in Fig. 8g. It was observed that the crack in the specimen appears approximately at the same instance when the DCZM elements start to reach its peak value ( $F_{max}$ ) in the DCZM simulation. As soon as the crack appears in the

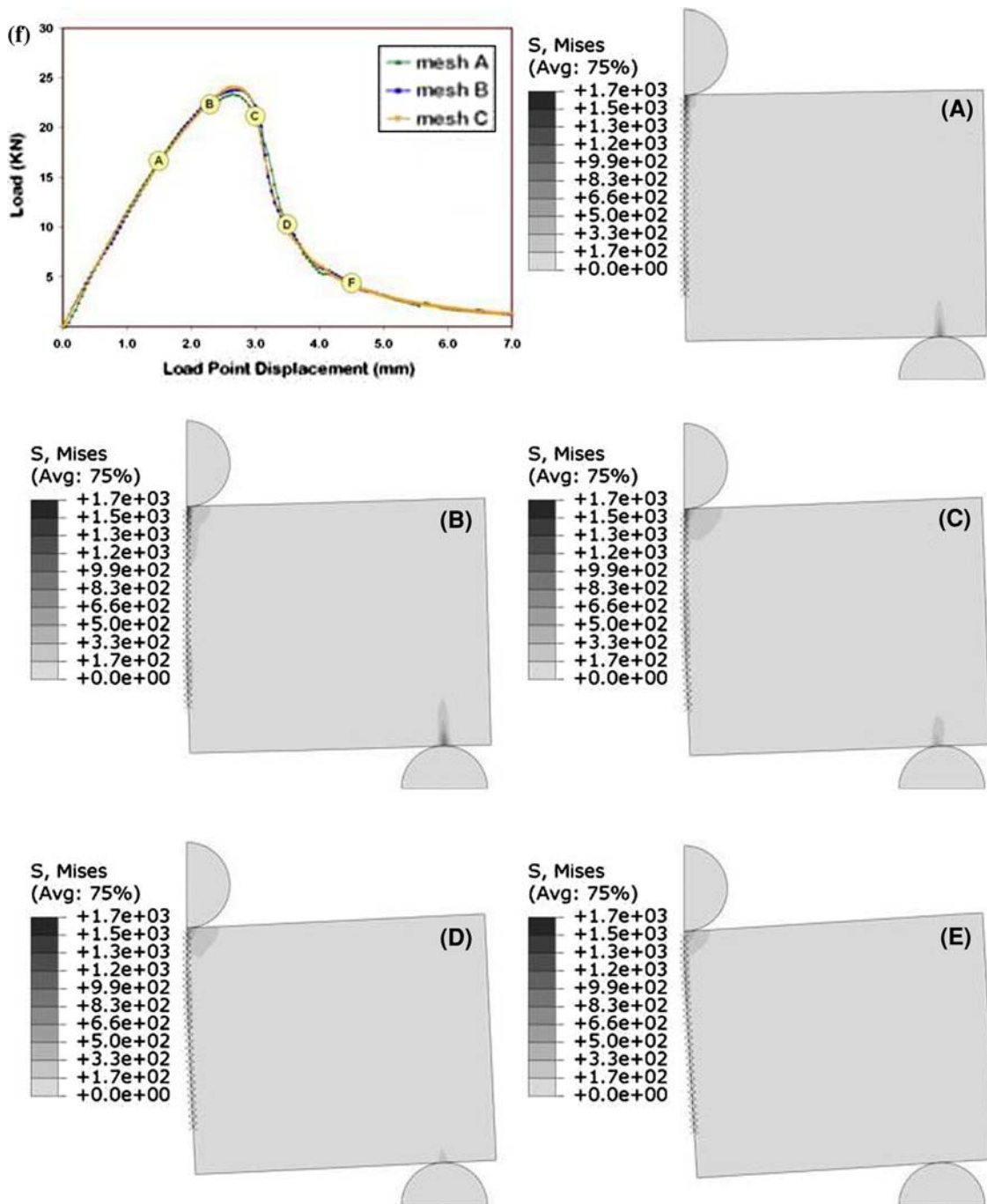


Fig. 8 continued

specimen, it is bridged by the biased tows (that are aligned at 45° to the crack) in the specimen. On further loading, this bridging zone starts to fail absorbing fracture energy. The failure of the bridging zone thus corresponds to DCZM elements in the region between  $F_{max}$  and  $F_{zero}$  as shown in Fig. 8g. For an increment of  $\Delta = 3$  mm (point C in Fig. 8f), the displacements of all the DCZM elements were

plotted. The limit of  $F_{max}$  and  $F_{zero}$  are also indicated in the plot. It is observed that near the crack tip some DCZM elements have already failed, while at the far end of the notch (near the loading point), the DCZM elements are yet to be loaded. The DCZM elements corresponding to the region between these two extremes are subjected to bridging forces that are in between of  $F_{max}$  and  $F_{zero}$ . This

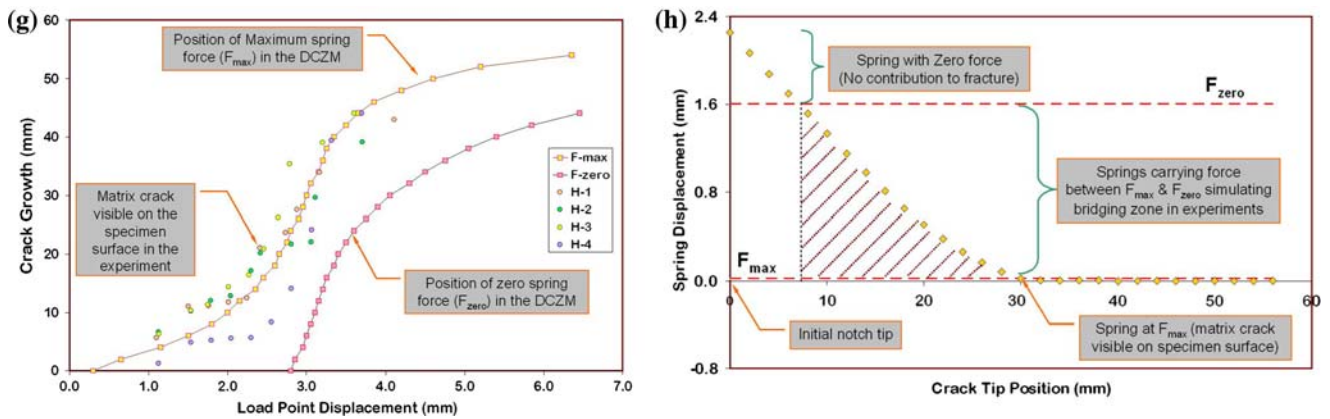


Fig. 8 continued

shaded area is the bridging zone on the specimen, which corresponds in length to about 22 mm for the Hetron specimens.

**Effect of resin on fracture of 2DTBC**

It was noted previously that Epon and Hetron 2DTBC specimens show significant difference in the stiffness values (refer Table 1) even though the virgin matrix properties reported by the manufacturer are very similar. These results were investigated and were observed to be closely related to the microstructure of the manufactured 2DTBC composites. This difference in microstructure affects the damage energy absorption in these composites as was seen earlier.

**Scanning electron microscope imaging**

Scanning electron microscope (SEM) cross-sectional images of 2DTBC Hetron specimens show poor wetting than Epon specimens. They are also seen to contain more voids. It is observed that in the Hetron specimens the axial tows were not fully wetted inside the fiber tow as shown in Fig. 9a. When pure Hetron resin was prepared in the laboratory, it displayed substantial shrinking during curing. As the resins are injected in braided fiber mats, it flows through all the pockets in between axial and bias tows. The matrix also penetrates the tows thus wetting it. As the Hetron resin starts to cure, it shrinks, thus flowing out of the tows back into the resin pockets. This is not seen in Epon specimens.

The specimens were also cut and polished along the length of the axial fiber tow as shown in Fig. 9b. Figure 9c shows the comparison between Hetron and Epon specimens. It is clearly observed that the axial tows in the

Hetron specimens are not wetted completely in the center. Figure 9d shows the center of the axial tow of the Hetron specimen. The matrix has not penetrated the axial tow in the Hetron specimens. Figure 9e shows the cross section of a biased tow in the composite. It is seen that the biased tows in Hetron specimens are cracked due to residual stress. These cracks are absent in the Epon specimens which show good wetting and minimal effects at curing. Due to the relatively large shrinkage of the Hetron resin, the in situ Hetron matrix is under a tensile residual stress state, while in the Epon composite such a prominent residual stress state is absent (the fibers act as “obstacles” to prevent the Hetron from shrinking, forcing it to a state of residual tension). The tensile residual stress state leads to poor wetting and a larger initial void content than in Epon composites. Due to the higher void content, the Hetron matrix starts to crack prematurely (matrix micro-cracking), which causes the damage to spread in the specimens (leading to larger strains) resulting in higher energy absorption. Thus it is important to compare the void content and the extent of wetting in these specimens. Quantitatively these effects are captured through the “in situ” properties of the resin, extracted from tests done with the cured 2DTBC. These effects can also play a significant role in influencing energy absorption in structural scaling studies [28].

**Concluding remarks**

A generalized methodology to predict fracture in non-homogeneous and orthotropic 2D triaxially braided composites is presented. Static fracture tests were carried out on carbon fiber braided composites specimens by cyclically and monotonically loading notched CTS. Load and load-point displacement and the crack propagation during the

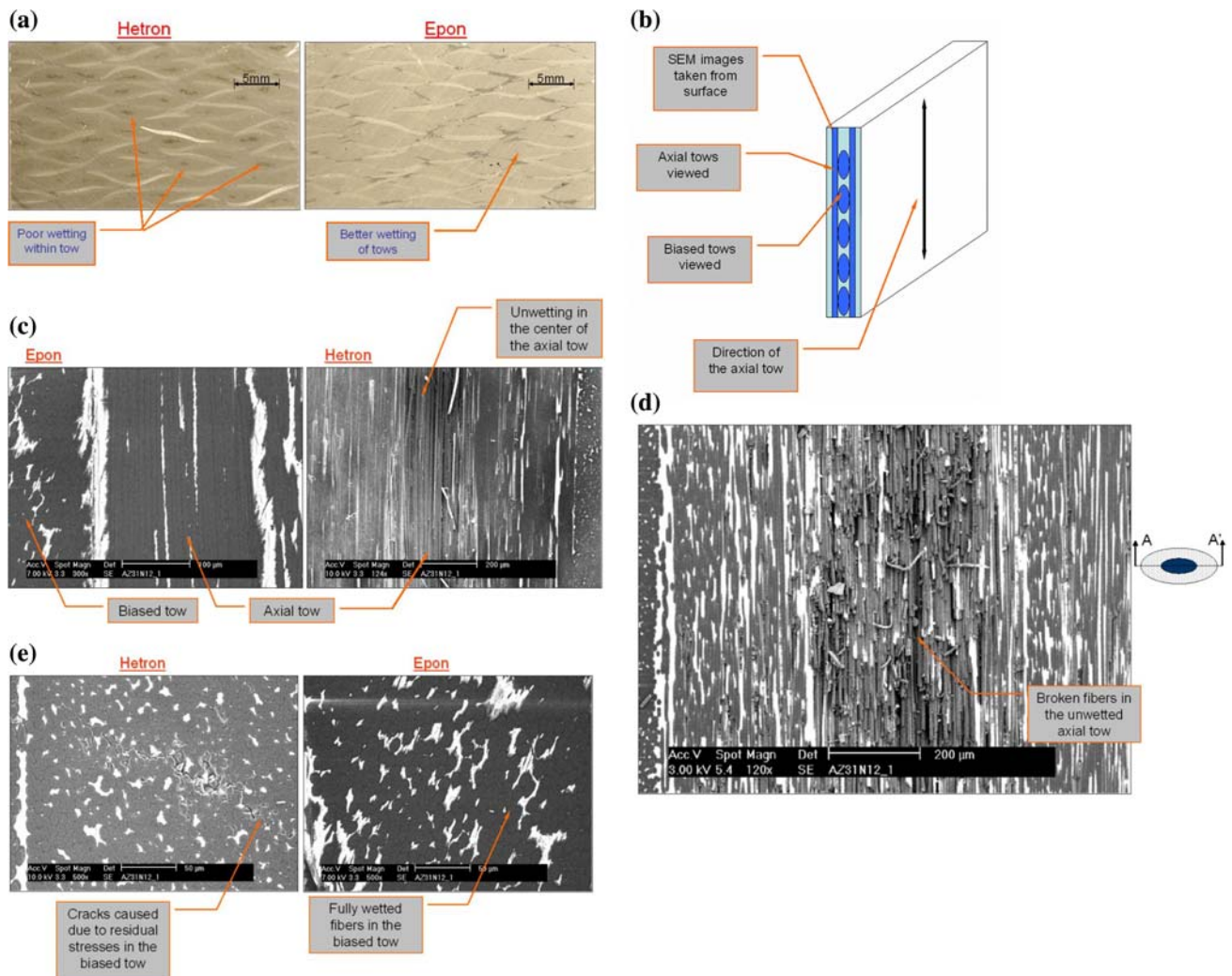


**Fig. 9** (a) Comparison of Hetron and Epon specimen cross sections observed under microscope. (b) Schematic of specimens cutting and area observed under SEM. (c) Comparison of axial tows between

Hetron and Epon specimens. (d) Unwetted center of the axial tow of the Hetron specimen. (e) Cross section of a biased tow show crack in the Hetron matrix

loading were measured. In cyclic loading, fracture energy ( $G_{Ic}$ ) was calculated for each cycle by using this information. It was found that this method gives non-uniform fracture energy as a function of crack position, which could not be effectively used for numerical analysis, thus a different approach was needed to measure the fracture energy. Fracture tests were then carried out by loading the CTS specimens monotonically to failure. Fracture energy ( $G_{Ic}$ ) was calculated by measuring the area under the  $P-\Delta$  curve and then dividing by the total crack extension. This approach gives an averaged fracture energy (essentially averaging the crack growth path over several lengths of the scale of non-homogeneity in these classes of material).

A DCZM was implemented to predict fracture and damage growth in these materials. Specimen geometry, material properties, fracture energy, and cohesive strength values were used as inputs in the DCZM. These inputs

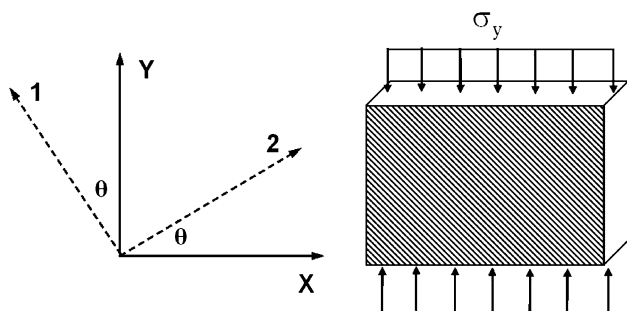
(fracture energy and cohesive strength) were measured using CTS tests and double-notched tension tests, respectively. With these inputs in hand, the DCZM was used to *predict* the response of Hetron and Epon composites in an SETB configuration. The SETB test results were repeatable in terms of the  $P-\Delta$  response. It is noted that the CTS and SETB tests were carried out using similar size specimens. Scaling of the proposed methodology to specimens of different sizes is also an aspect that remains to be investigated. The DCZM predictions were found to be in good agreement with measured  $P-\Delta$  response of the SETB tests. Microstructural effects such as matrix void contents, residual matrix stresses, etc., observed in the specimens are captured in the measured fracture energy ( $G_{Ic}$ ) and cohesive strength ( $\sigma_c$ ), and are reflected at a structural level through the DCZM simulations. In essence, the in situ matrix properties are indirectly incorporated into the

characterization of  $G_{Ic}$ ,  $\sigma_c$ , and the plasticity parameter,  $a_{66}$ . Thus, the proposed methodology can be used with confidence to understand and predict the mechanical response, damage tolerance, and damage growth in load bearing textile composite structural components.

**Acknowledgements** The authors are grateful for the financial sponsorship of the Automotive Composites Consortium, Energy Management Working Group, and the Department of Aerospace Engineering, University of Michigan. The authors acknowledge that this research was supported, in whole or in part, by Department of Energy cooperative agreement no. DE-FC05-95OR22363. Such support does not constitute an endorsement by the Department of Energy of the views expressed herein.

**Appendix: measurement of the plasticity parameter  $a_{66}$**

The plastic response of braided composites was characterized by carrying out off-axis compression tests. Rectangular composite coupons were cut in such a way that the axial fiber tow makes an angle with the direction of loading as shown below.



A three-strain gage rosette was used to measure the global strains that are then transformed to get the local strains in the specimen principal material directions. Axial stress is also measured during the test. A yield function or plastic potential that is quadratic in stresses for an orthotropic composite gives an equivalent stress and a work conjugate equivalent plastic strain as

$$\bar{\sigma} = \sqrt{\frac{3}{2} (a_{22}\sigma_{22}^2 + 2a_{66}\sigma_{12}^2)}, \tag{6a}$$

$$d\bar{\epsilon}^p = \frac{2}{3} (a_{22}\sigma_{22}^2 + 2a_{66}\sigma_{12}^2) d\lambda, \tag{6b}$$

$$d\lambda = \frac{3}{2} \left( \frac{d\bar{\epsilon}^p}{d\bar{\sigma}} \right) \left( \frac{d\bar{\sigma}}{\bar{\sigma}} \right), \tag{6c}$$

where,  $\bar{\sigma}$  is the Von Mises type equivalent stress,  $d\bar{\epsilon}^p$  is the equivalent plastic strain increment, and  $d\lambda$  is a scalar factor of proportionality. The parameters  $a_{22}$  and  $a_{66}$  are the material constants that characterize orthotropy of the plastic response.

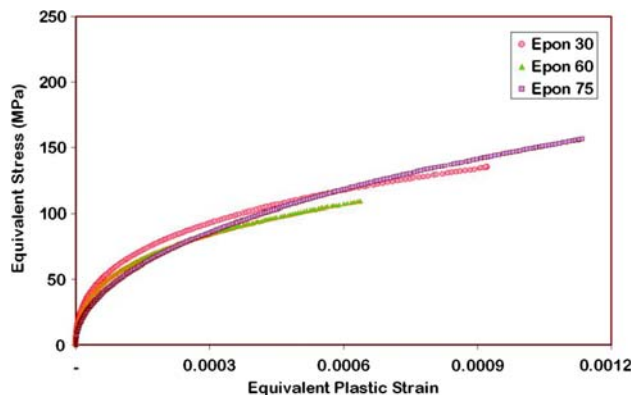


**Fig. 10** Collapsed equivalent stress versus equivalent plastic strain Epon specimen ( $a_{66} = 1.1$ )

Substituting, using stress transformations, into Eq. 6a–c to specialize to the off-axis compression test configuration, results in

$$\bar{\sigma} = \sqrt{\frac{3}{2} (\sigma_y^2 n^4 + 2a_{66}\sigma_y^2 m^2 n^2)} \tag{6d}$$

or

$$\bar{\sigma} = \sigma_y h(\theta).$$

Similarly,

$$\bar{\epsilon}^p = \frac{\epsilon_y^p}{h(\theta)},$$

where,  $m = \cos(\theta)$ ,  $n = \sin(\theta)$ , and  $h(\theta) = \sqrt{\frac{3}{2} (n^4 + 2a_{66}m^2 n^2)}$ .

Off-axis tests were carried out on 30, 60, and 75° specimens. Thus, from experimental measurement of  $\sigma_y$  and  $\epsilon_y$ , the equivalent stress and equivalent plastic strain are plotted for every off-axis angle. For each test, a value of  $a_{66}$  is selected such that the curves of equivalent stress versus equivalent plastic strain for each off-axis angle collapses to one. Test data for different off-axis angles for Epon specimens are given in Fig. 10. The value of  $a_{66}$  corresponding to this converged behavior was found to be 1.1. Similarly, value of  $a_{66}$  for Hetron specimens was found to be 1.2.

**References**

1. Beard SJ, Chang FK (2002) Int J Crashworthiness 7(2):191. doi: 10.1533/cras.2002.0214
2. Quek SC, Waas AM, Shahwan KW, Agaram V (2003) Int J Mech Sci 45(6–7):1077. doi:10.1016/j.ijmecsci.2003.09.003
3. Haywood JB (2006) Sci Am 295(3):94
4. Reifsnider KL, Case SW (2002) Damage tolerance and durability of material systems. Wiley
5. Gonzales L, Knauss WG (2002) Int J Fract 118(4):363. doi: 10.1023/A:1023351115322



6. Hertzberg J (1983) Deformation and fracture mechanics of engineering materials. Wiley
7. Xie D, Biggers SB Jr (2006) *Eng Fract Mech* 73:771. See also, Xie D, Biggers SB Jr (2006) *Finite Elem Anal Design* 42(11):977. doi:[10.1016/j.finel.2006.03.007](https://doi.org/10.1016/j.finel.2006.03.007)
8. Xie D, Biggers SB Jr (2006) *Eng Fract Mech* 73:786. doi:[10.1016/j.engfracmech.2005.07.014](https://doi.org/10.1016/j.engfracmech.2005.07.014)
9. Xie D, Waas AM, Shahwan KW, Schroeder JA, Boeman RG (2004) *Comput Model Eng Sci* 6:515
10. Xie D, Waas AM (2006) *Eng Fract Mech* 73:1783. doi:[10.1016/j.engfracmech.2006.03.006](https://doi.org/10.1016/j.engfracmech.2006.03.006)
11. Xie D, Chung J, Waas AM, Shahwan KW, Schroeder JA, Boeman RG, Kunc V, Klett LB (2005) *Int J Fract* 134:231. doi:[10.1007/s10704-005-0646-y](https://doi.org/10.1007/s10704-005-0646-y)
12. Xie D, Salvi AG, Sun C, Waas AM, Caliskan A (2006) *J Compos Mater* 40:2025. doi:[10.1177/0021998306061320](https://doi.org/10.1177/0021998306061320)
13. Pietruszczak S, Mroz Z (1981) *Int J Numer Methods Eng* 17:327. doi:[10.1002/nme.1620170303](https://doi.org/10.1002/nme.1620170303)
14. Ungsuwarungsri T, Knauss WG (1987) *Int J Fract* 5:221. See also PhD Thesis (1985) Aeronautics Department, Caltech, Pasadena, CA
15. Tvergaard V, Hutchinson JW (1992) *J Mech Phys Solids* 40:1377. doi:[10.1016/0022-5096\(92\)90020-3](https://doi.org/10.1016/0022-5096(92)90020-3)
16. Schellekens JCJ, de Borst R (1993) *Int J Numer Methods Eng* 36:43. doi:[10.1002/nme.1620360104](https://doi.org/10.1002/nme.1620360104)
17. Xu XP, Needleman A (1994) *J Mech Phys Solids* 42:1397. doi:[10.1016/0022-5096\(94\)90003-5](https://doi.org/10.1016/0022-5096(94)90003-5)
18. Camacho GT, Ortiz M (1996) *Int J Solids Struct* 33:2899. doi:[10.1016/0020-7683\(95\)00255-3](https://doi.org/10.1016/0020-7683(95)00255-3)
19. Reedy ED, Mello FJ, Guess TR (1997) *J Compos Mater* 31:812
20. Pandolfi A, Krysl P, Ortiz M (1999) *Int J Fract* 95:279. doi:[10.1023/A:1018672922734](https://doi.org/10.1023/A:1018672922734)
21. Espinosa HD, Zavattieri PD, Dwivedi SK (1998) *J Mech Phys Solids* 46:1909. doi:[10.1016/S0022-5096\(98\)00027-1](https://doi.org/10.1016/S0022-5096(98)00027-1)
22. Zavattieri PD, Raghuram PV, Espinosa HD (1002) *J Mech Phys Solids* 49:27
23. Li S, Thouless MD, Waas AM, Schroeder JA, Zavattieri PD (2006) *Eng Fract Mech* 73:64
24. Gustafson PA, Waas AM (2007) “Experimental results and numerical analysis of high temperature bonded composite joints: Kriging sensitivity analysis of common adhesive tests”. ASME Congress presentation, November
25. Anderson TL (1995) *Fracture mechanics*, 2nd edn. CRC Press LLC
26. Salvi AG, Waas AM, Caliskan A (2004) *Polym Compos* 25(4):397
27. Salvi AG, Waas AM, Caliskan A (2004) *Compos Sci Technol* 64:83
28. Turner TA, Warrior NA, Robitaille F (2005) *Compos A Appl Sci Manuf* 36(9):1291